

Article

# Comparative Evaluation of High-Speed Bearingless Cross-Flow Fan Designs for Lithography Excimer Lasers

Ivana Bagaric <sup>1,\*</sup> , Rennan Hu <sup>2</sup>, Daniel Steinert <sup>2</sup>, Thomas Nussbaumer <sup>2</sup> and Johann Walter Kolar <sup>1</sup><sup>1</sup> Power Electronic Systems Laboratory, ETH Zurich, 8092 Zurich, Switzerland; kolar@lem.ee.ethz.ch<sup>2</sup> Levitronix GmbH, 8048 Zurich, Switzerland; rennan.hu@levitronix.com (R.H.); steinert@levitronix.com (D.S.); nussbaumer@levitronix.com (T.N.)

\* Correspondence: bagaric@lem.ee.ethz.ch

**Abstract:** This study conducted a comparative evaluation of two bearingless cross-flow fan designs for applications in deep ultraviolet lithography excimer lasers, where maximizing the speed and power of the fan has a direct influence on the throughput and scanning speed of these devices. Using bearingless motor technology enables a combined generation of bearing force and drive torque and leads to a compact, hermetically sealed, and conveniently maintainable drive system. With identical bearingless motors on both rotor sides, it is possible to drive the cross-flow fan symmetrically to high rotational speeds at low torsional loads. The rotor prototypes were optimised, analysed, and pushed to high-speed operation and evaluated with respect to their rotor dynamic and fluid dynamic performance using finite element methods and experimental measurements. For both prototypes, successful numerical studies were performed, where a modal analysis enabled theoretical predictions of expected resonance frequencies, and a CFD analysis visualised local flow effects and provided cross-flow fan design comparisons. A stable operation of up to 12,000 rpm and 5500 rpm was accomplished for the two elaborated designs.

**Keywords:** bearingless motors; cross-flow fan; DUV excimer laser; rotor dynamics; fluid dynamics; CFD



**Citation:** Bagaric, I.; Hu, R.; Steinert, D.; Nussbaumer, T.; Kolar, J.W. Comparative Evaluation of High-Speed Bearingless Cross-Flow Fan Designs for Lithography Excimer Lasers. *Machines* **2023**, *11*, 611. <https://doi.org/10.3390/machines11060611>

Academic Editor: Mohammadreza Ilkhani

Received: 29 April 2023

Revised: 26 May 2023

Accepted: 30 May 2023

Published: 2 June 2023



**Copyright:** © 2023 by the authors. Licensee MDPI, Basel, Switzerland. This article is an open access article distributed under the terms and conditions of the Creative Commons Attribution (CC BY) license (<https://creativecommons.org/licenses/by/4.0/>).

## 1. Introduction

Components in microelectronics have been becoming increasingly smaller, and this trend will continue in the future. Complex fabrication methods are needed to meet the evolving requirements of current state-of-the-art microchips. Highly specialized laser modules, such as short-wavelength deep ultraviolet (DUV) lithography systems, are used to burn in nanometre-scale features [1]. Figure 1a shows a schematic of such a system that typically contains an ArF or KrF excimer laser as its light source [2]. The throughput of these lasers, and thus the scanning speed of the system, is, among other factors, limited by the performance of the cross-flow fan (CFF) contained in the laser [1,3–6]. This paper conducts a comparative evaluation of bearingless CFF designs for such applications. Two designs are analysed in terms of rotor dynamic and fluid dynamic performance using finite element methods (FEM) and experimental measurements and pushed to high-speed operation.

The cross-section of such a laser is shown in Figure 1b, where the main components are electrodes for the electrical discharge, heat exchangers to remove excess heat, and the CFF. The main task of the CFF is the continuous renewal of the laser gas between the electrodes. Since the gas mixture in the discharge region has to be replaced before the next laser pulse can be generated, the maximum achievable repetition rate, and thus, the throughput of the laser, depends directly on the flow rate generated by the cross-flow fan [1]. This relationship is described by the flow-clearing ratio,  $C$ :

$$C = \frac{v}{w \cdot f} \quad (1)$$

where  $v$  is the gas flow velocity between electrodes,  $w$  is the discharge width, and  $f$  is the repetition rate of the laser (see Figure 1b) [1]. Clearing ratios of

$$C_{\min} > 2 - 3 \quad (2)$$

are required to enable the successful generation of the next laser pulse [1]. The throughput is then calculated from the energy per pulse, and the repetition rate is calculated as

$$P_{\text{out}} = E_{\text{pulse}} \cdot f. \quad (3)$$

High repetition rates  $f$  at moderate pulse energies  $E_{\text{pulse}}$  are demanded, resulting in high scan speeds, good energy stability, and compact designs [2]. Increasing the repetition rate leads to further improvements in these properties, which can be accomplished by increasing the CFF's rotational speed, thereby increasing the flow velocity. This means that a high-speed CFF is a direct enabler of improved laser performance. The industry, technology, and laser requirements are summarised in Figure 1c.

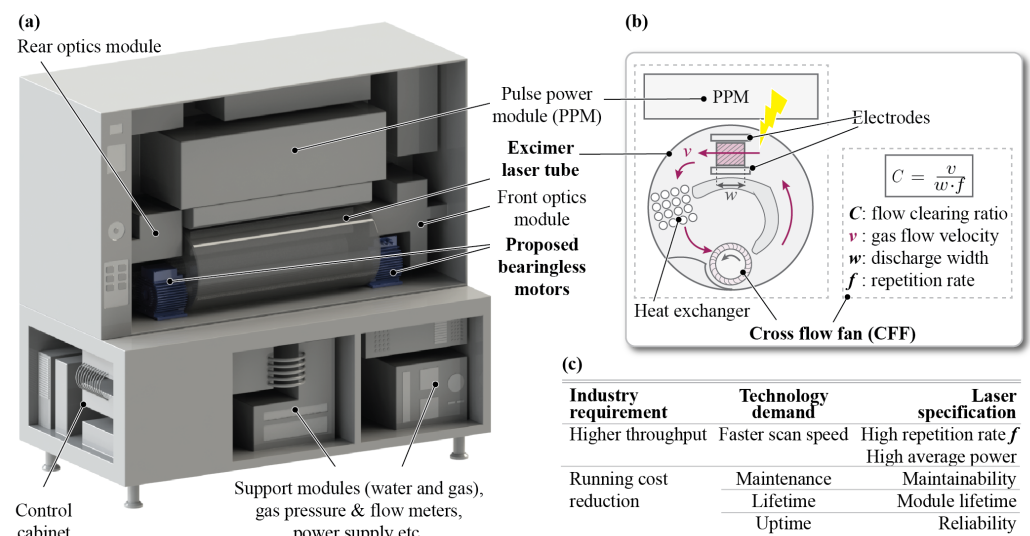


**Figure 1.** (a) Conceptual drawing of a deep ultraviolet (DUV) lithography system with an ArF or KrF excimer laser as the light source. (b) Cross-section of an excimer laser chamber with the electrodes, heat exchangers, and the CFF as its main components. (c) Summary of key industry requirements, technology demands, and laser specification.

The state-of-the-art in this type of DUV excimer laser is the implementation of magnetically supported CFFs. There are several patents for active magnetic bearing systems used for the contactless levitation of CFFs [7–9]. Conventional magnetic bearings require at least two radial bearings and one axial bearing to fully stabilise the rotor, in addition to a motor to generate the drive torque, as illustrated in Figure 2a. For the laser application at hand, this magnetic bearing concept offers the advantage of no friction, no wear, and a hermetic encapsulation of the rotor when dealing with the extremely toxic and corrosive excimer gases. However, it is limited in terms of performance due to its one-sided torque generation and the occurrence of high torsional loads, which reduce the lifetime of the fan system. As highlighted in Figure 2a, the complex air gap geometry and encapsulation of the rotor limit the design in terms of compactness and safety and make maintenance work on these systems very inconvenient.

The bearingless motor concept for the CFF application, as presented in this paper, is shown in Figure 2b. An absolute hermetic sealing is enabled as the integration of the motor and magnetic bearing in one compact unit maximizes the air gap and thus the space for the insulation layer [10–14]. Furthermore, this technology reduces the space required for the bearing and drive system since, instead of two radial bearings, one axial bearing

and one motor (as with the conventional magnetic bearings seen in Figure 2a), only two compact bearingless motors are required. Another unique technical advantage is that the CFF rotor is driven symmetrically from both sides without requiring additional space or components. Since CFFs have low torsional stiffness due to their construction, torsional loads and torsional vibrations are significantly reduced, which increases the performance of the bearingless fan system. The bearingless CFF concept was first presented by the authors in [15] for a conceptual prototype up to 3500 rpm. For DUV excimer lasers, the bearingless CFF design enables a highly compact, hermetically sealed and safe placement of the motors outside the laser chamber, which contains toxic and corrosive gases. This massively improves the safety standard, simplifies new installations and costly maintenance work, and increases the lifetime of the fan system. Due to its high drive power, which is available on both rotor sides, the speed and, thus, the generated flow of the fan can be increased, which has a direct influence on the repetition rate of the laser.

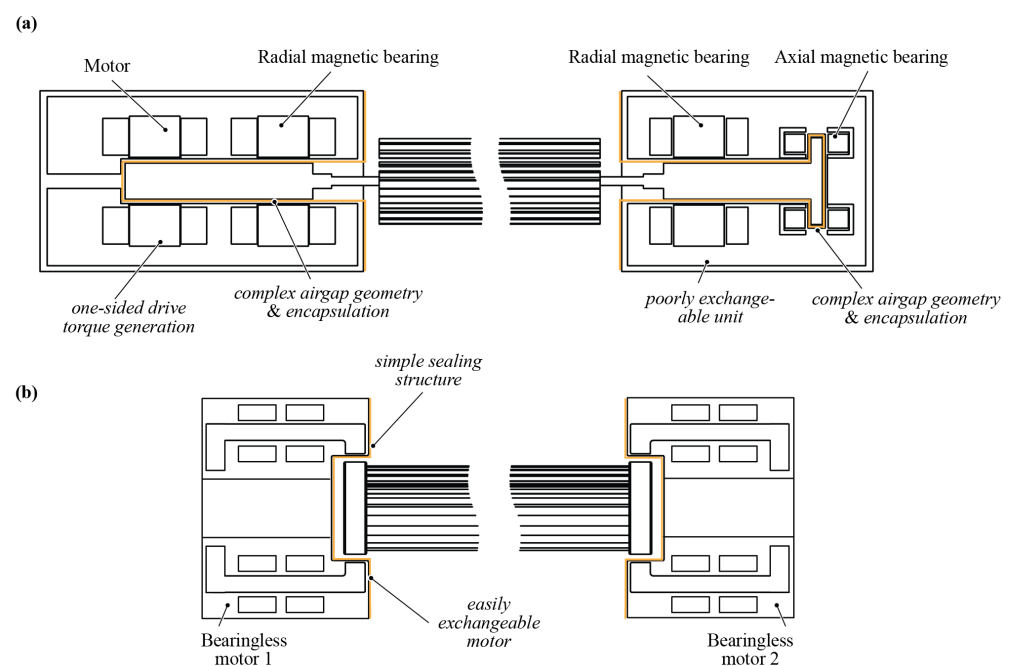


**Figure 2.** CFF levitated and rotated (a) by a magnetic bearing system including two radial magnetic bearings, one axial magnetic bearing, and a drive system and (b) by two bearingless motors.

The challenges in implementing a bearingless high-speed and high-performance CFF lie particularly in the rotor and fluid dynamic behaviour, the influence on the magnetic bearing, and the high power demand for the driving motors. The rotor has to be mechanically designed for high speeds and high flows simultaneously, while the magnetic bearing has to be able to withstand these forces. The goal of this paper is to design, optimise, and analyse two prototypes and to push them to high rotational speeds. The rotor designs shall be evaluated in terms of rotor and fluid dynamic behaviour by means of FEM simulations and experimental measurements within a constructed test rig.

In Section 2, the bearingless motor and its operating principle are described. Subsequently, two rotor prototypes, where one is a single-body aluminium rotor with straight fan blades and the other is a multi-body stainless-steel rotor with curved fan blades, are presented in Section 3 and are compared in Section 4 with respect to their rotor dynamic behaviours. A detailed numerical study of the fluid dynamic aspects of both rotors follows in Section 5. Finally, the designed test rig and the experimental results are presented in Section 6.

## 2. Bearingless Motor Topology

The bearingless motor topology proposed for the high-speed and high-performance CFF application is illustrated in Figure 3a. Magnetic bearing and drive forces are transmitted via a common iron circuit to the rotor, which features a one-pole-pair permanent magnet on each side. Due to this so-called temple design, the magnetic field is generated outside the rotor planes, resulting in a very compact shape of the motor. The simple air gap geometry enables a conveniently maintainable, compact, and hermetically sealed implementation of the drives outside the laser chamber. The presented concept with bearingless motors used on both sides is also characterised by the high power available and low torsional load on the cross-flow fan blades. The most important motor controller data are summarised in Figure 3b.

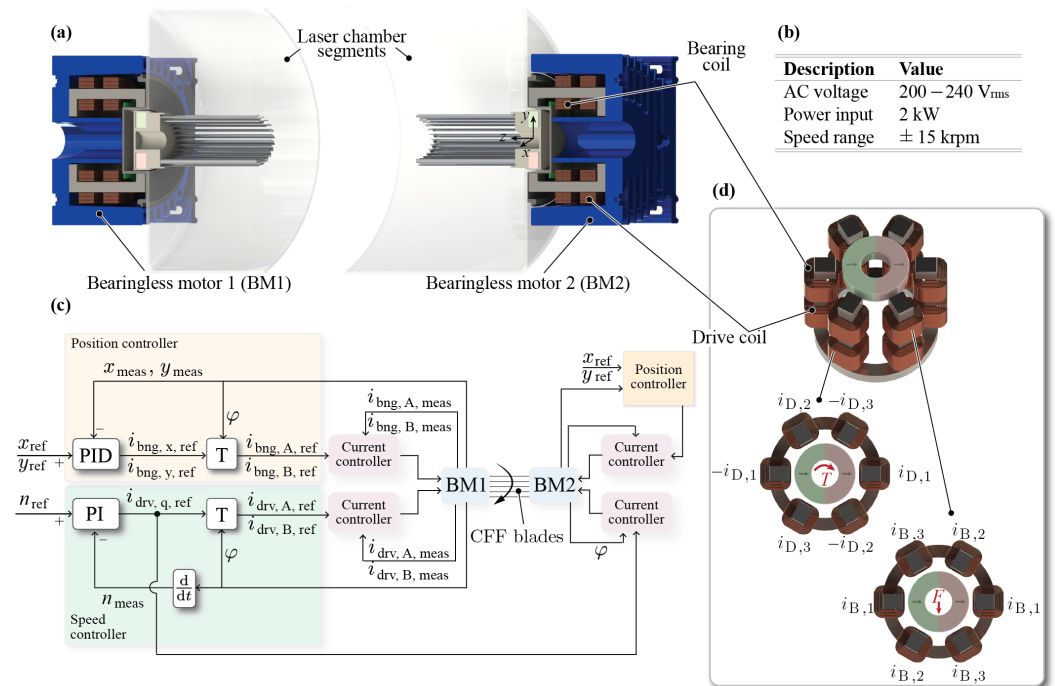


**Figure 3.** (a) Schematic cross-section of the bearingless CFF system in a DUV laser chamber. (b) Key parameters of the motor. (c) Control concept of the bearingless drives, where motor 1 (BM1) and motor 2 (BM2) control the bearing forces individually. Both bearingless motors receive a reference drive torque current from a single speed controller, which is implemented here in the “primary” motor BM1. Thereby, each motor generates half of the required drive torque, and the load is evenly distributed among BM1 and BM2 since they share a common rotor. Each motor handles the control of the drive phase currents separately, using its own angular sensor system. (d) Required coil currents for bearing force and drive torque creation. By applying equal currents (in magnitude and sign) to opposite bearing coils, radial forces are created. By applying currents to opposite drive coils with the same magnitude but opposite sign, tangential forces are generated, resulting in rotor torque.

The operating principle of the bearingless motor can be explained with Figure 3c,d and is described in detail in [16]. By applying equal currents (in magnitude and sign) to opposite bearing coils (see Figure 3d), a two-pole-pair stator field is created, which, together with the rotor field, generates radial forces. By applying currents to opposite drive coils with the same magnitude but opposite sign, a single-pole-pair stator field is generated, which is 90° ahead of the rotor field. These tangential forces create a rotor torque. Stabilisation in the axial z-direction is achieved by passive reluctance forces between the magnet and the surrounding iron yoke; hence, no additional axial bearing is necessary.

Figure 3c shows how the control of a common CFF rotor via two bearingless motors has been implemented. Bearingless motor (BM) 1 and BM2 control the bearing forces independently using a cascaded PID control structure. The torque is generated by both

motors by passing a reference torque current from BM1 (“primary”) to BM2 (“secondary”), i.e., each motor contributes half of the required drive torque, such that the load is evenly distributed. The control of the drive phase currents is handled by each motor separately using its own angular sensor system. The speed control is handled by BM1 through a PI controller. This means that high drive forces are available on both rotor sides, which massively reduces torsional loads on the rotor.

For the intended high-speed application, the bearingless CFF system presented here is an ultra-compact, conveniently exchangeable and maintainable, and safe option designed for high performance.

### 3. High-Speed Rotor Prototypes

The goal of this paper is firstly to select CFF rotor designs that allow high rotational speeds due to their high mechanical strength, that are manufacturable, and that generate high flow rates and to then investigate them by means of FEM simulations and experimental measurements. The focus lies on the rotor dynamic and fluid dynamic behaviour. The challenge is to find a trade-off between mechanical strength and fluid performance since, on the one hand, designs that increase strength come at the expense of fluid inlet area or disrupt the flow through the fan, resulting in a reduction in fluid performance. On the other hand, thin fan blades allow for high fluid performance, but from a mechanical point of view, they limit the achievable rotational speed.

The two chosen prototypes are shown in Figure 4, and their main mechanical characteristics are summarised in Table 1. Prototype 1 (PT1) is a CFF rotor milled from a full cylinder of aluminium, which is mechanically robust and stiff. To limit the manufacturing complexity, the blade surface geometry is kept straight, and the thickness of the individual blades is relatively high at 1.4 mm, to the disadvantage of the fluid inlet area.

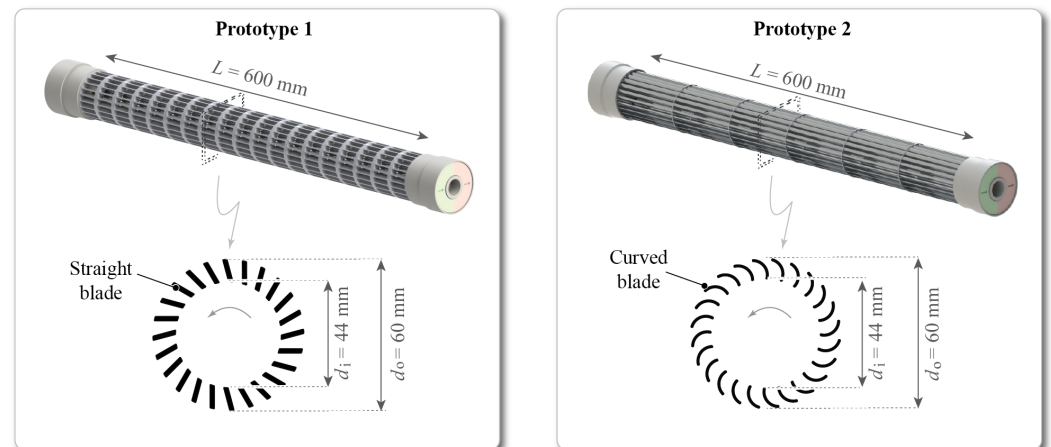


**Figure 4.** Renderings of the investigated prototypes (PTs). Single-body PT1 consists of 1.4 mm thick, straight aluminium blades, and the multi-body PT2 consists of 0.5 mm thin, curved, stainless-steel blades.

**Table 1.** Table with key parameters of the investigated CFF prototypes.

	Prototype 1	Prototype 2
Material	Aluminium	Stainless steel
Mass of CFF blades	890 g	740 g
Total length $L_{tot}$	680 mm	680 mm
Fluid inlet length $L_{fluid}$	400 mm	590 mm
Outer diameter $d_o$	60 mm	60 mm
Inner diameter $d_i$	44 mm	44 mm
Cross-sectional blade profile	Straight	Curved
Blade thickness	1.4 mm	0.5 mm

Having the same external dimensions, Prototype 2 (PT2) consists of individual 0.5 mm thin, curved, stainless-steel blades connected to separation plates. While this design is advantageous for fluid performance, its mechanical stiffness is heavily reduced, and some uncertainty occurs when modelling the multi-body fan.

The selected PTs with respect to high-speed and high-performance applications were evaluated through simulations and experiments and compared in terms of their rotor dynamic and fluid dynamic behaviour. The applied methods are described in detail in the next sections.

#### 4. Rotor Dynamical Analysis

The rotor dynamic behaviour of the system was investigated to achieve the desired CFF speed range since the magnetic bearing can only handle forces and allow displacements to a limited extent. The aim was to design a rotor that is mechanically robust for high speeds and whose destabilising dynamic forces can be controlled by the magnetic bearing.

##### 4.1. Analytical Description

The Jeffcott rotor model was used for the mathematical description and explanation of important rotor dynamic effects. This model of rotor dynamics can be extended from a rigid, mechanically supported system to a two-sided, magnetically levitated elastic rotor. For the investigated case of a two-sided, magnetically levitated elastic CFF, the model of the Jeffcott rotor shown in Figure 5b was used, which is explained in more detail in [17]. The model consists of a disc with mass  $m_R$  and mass eccentricity  $\epsilon$ , two magnets in the magnetic bearing (MB) with mass  $m_B$ , and a massless shaft with bending stiffness  $k_{\text{shaft}}$ . If the magnets in the MB are attributed their own degrees of freedom  $w_R(t)$  and  $w_B(t)$  and the magnetic bearing is assumed to be rotationally symmetrical, then the radial displacement of the bearing magnets  $r_B(t)$  and radial displacement of the geometric disc centre  $r_R(t)$  can be expressed in a complex manner, as follows:

$$\begin{aligned} r_R(t) &= w_R(t) + jv_R(t) \\ r_B(t) &= w_B(t) + jv_B(t). \end{aligned} \quad (4)$$

This relationship is illustrated in Figure 5a. The following equations of motion are obtained for this system:

$$\mathbf{M} \begin{Bmatrix} \ddot{r}_R \\ \ddot{r}_L \end{Bmatrix} + \mathbf{D} \begin{Bmatrix} \dot{r}_R \\ \dot{r}_L \end{Bmatrix} + \mathbf{K} \begin{Bmatrix} r_R \\ r_L \end{Bmatrix} = \epsilon m_R \Omega^2 \begin{Bmatrix} e^{j\Omega t} \\ 0 \end{Bmatrix}. \quad (5)$$

The mass matrix  $\mathbf{M}$  is composed of the disc mass  $m_R$  and the two magnet masses  $m_B$  according to

$$\mathbf{M} = \begin{bmatrix} m_R & 0 \\ 0 & 2 \cdot m_B \end{bmatrix}. \quad (6)$$

The damping

$$\mathbf{D} = \begin{bmatrix} 0 & 0 \\ 0 & 2 \cdot D \cdot k_i \end{bmatrix} \quad (7)$$

and stiffness matrices

$$\mathbf{K} = \begin{bmatrix} k_{\text{shaft}} & -k_{\text{shaft}} \\ -k_{\text{shaft}} & k_{\text{shaft}} + 2(P \cdot k_i - k_s) \end{bmatrix} \quad (8)$$

include the PD control parameters of the active magnetic bearing with position-proportional feedback (P-element)

$$P = \frac{k_{\text{bng}} + k_s}{k_i} \quad (9)$$

and velocity-proportional feedback (D-element)

$$D = \frac{d}{k_i} \tag{10}$$

The parameters  $P$  and  $D$  are determined by setting appropriate values for stiffness  $k$  and damping  $d$  of the closed-loop system [18]. Moreover, the radial bearing stiffness (force/displacement factor) is represented by  $k_s$ , and the active bearing force constant (force/current factor) is represented by  $k_i$ . Introducing the abbreviations

$$\begin{aligned} v &= m_B/m_R && \text{mass of bearing magnet/mass of disc} \\ a &= k_{bng}/k_{shaft} = 2(P \cdot k_i - k_s)/k_{shaft} && \text{Relation between magnetic bearing stiffness} \\ &&& k_{bng} \text{ and elastic shaft stiffness } k_{shaft} \\ b &= 2 \cdot D \cdot k_i/m_R \cdot \omega_{Jeffcott} && \text{related damping} \\ \omega_{Jeffcott} &= \sqrt{k_{shaft}/m_R} && \text{reference frequency} \end{aligned} \tag{11}$$

the eigenvalues of the homogeneous solution of the differential Equation (5) can be calculated as a function of the stiffness ratio  $a$ . The detailed derivation can be found in [17]. The most relevant conclusions about the relationship between resonance frequencies and magnetic bearing stiffness can be drawn from Figure 5c with exemplary values of  $v = 0.2$  and  $b = 0.5$ . For an elastic bearing with  $a < 0.5$ , the first natural frequency  $\omega_1$  represents the rigid body mode, and the second natural frequency  $\omega_2$  represents that of the free-free resonating shaft, i.e., the first bending resonance frequency. In the middle part,  $\omega_1$  and  $\omega_2$  are two “elastic” vibrations. The case of  $1/a$  approaching 0 represents a rigid bearing, with  $\omega_1$  as the first bending resonance frequency and  $\omega_2$  as the vibration at which  $m_B$  oscillates in a manner almost uninfluenced by the shaft stiffness  $k_{shaft}$  on the magnetic bearing stiffness  $P \cdot k_i - k_s$ .

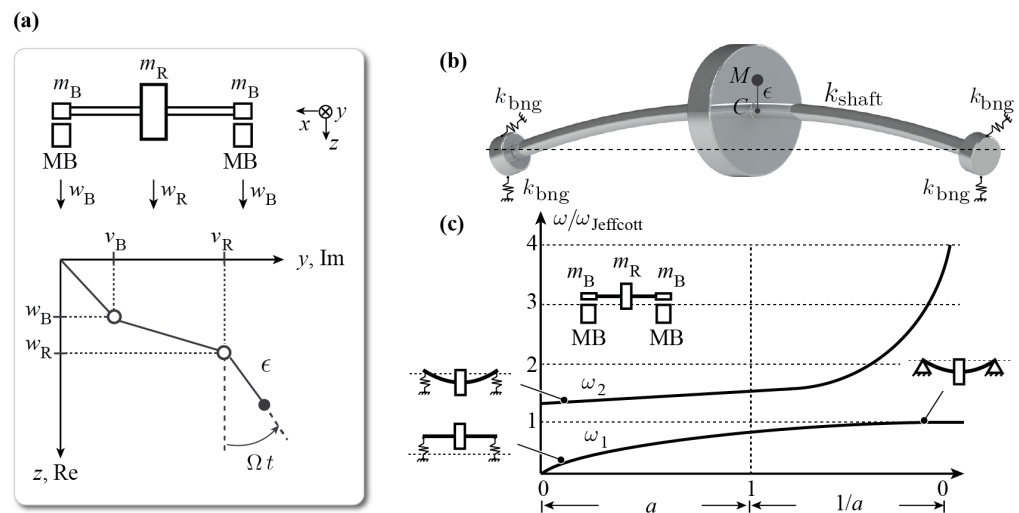


**Figure 5.** (a) Degrees of freedom of the two-sided magnetically levitated, elastic Jeffcott rotor model. (b) Rendering of the elastic Jeffcott rotor model in a magnetic bearing system. (c) Relationship of the system’s natural frequencies  $\omega_1$  and  $\omega_2$  with the stiffness ratio  $a = k_{bng}/k_{shaft}$ , where  $k_{bng}$  is the magnetic bearing stiffness and  $k_{shaft}$  is the shaft stiffness. In the region  $0 < a < 1$ , the magnetic bearing is weaker than the shaft, whereas in region  $1 < 1/a < \infty$ , the magnetic bearing is stiffer than the shaft. For the elastic rotor at hand ( $0 << k_{shaft} << \infty$ ),  $a = 0$  means  $k_{bng} = 0$ , which represents a free–free-supported elastic rotor, whereas having  $1/a = 0$  means  $k_{bng} \rightarrow \infty$ , which represents a rigidly supported elastic rotor.

In summary, two vibrational modes are derived with this model, whose natural frequencies depend on the magnetic bearing stiffness. For the CFF rotors investigated in

this work, the Jeffcott assumption of the massless shaft with an eccentric disc deviates from reality. Nevertheless, the lower rigid and higher bending mode natural frequencies shown in Figure 5c are expected to occur depending on the magnetic bearing's stiffness. The Jeffcott model enables the qualitative explanation of important rotor dynamic phenomena for the case of an elastic rotor in active magnetic bearings. For quantitative conclusions, a 3D FEM analysis was performed. In the next section, the implemented modal analysis is described, and a direct comparison of both prototypes is drawn.

#### 4.2. Simulated Modal Analysis

The goal of the modal analysis was to determine the system's expected natural frequencies up to the first bending resonance frequency. The radial position of the proposed CFF system was controlled separately and independently in BM1 and BM2. In order to enable an assessment of this control method for different vibration types, a modal analysis was, therefore, important to estimate the expected resonance frequencies.

Modal analysis is, by definition, an analysis of linear dynamics based on the equation of motion with unknown displacement, velocity, and acceleration. It is assumed that in the equation of motion the external load equals 0 since natural frequencies and mode shapes are independent of the load. In addition, damping effects are neglected; hence, a free and undamped system is assumed, resulting in the eigenvalue problem

$$(\mathbf{K} - \omega_i^2 \mathbf{M}) \{\phi\}_i = \{0\} \quad (12)$$

with eigenvalues  $\omega_i$  and eigenvectors  $\phi_i$ . This system of equations is subjected to the performed 3D FEM model to determine the mode shape  $\{\phi\}_i$  and the associated frequency  $f_i = \omega_i / (2\pi)$ .

The Campbell diagrams resulting from the modal analysis are shown in Figure 6a for PT1 and in Figure 6b for PT2; they show the expected vibration modes and possible excitation orders up to the first bending resonance frequency. The unbalance excitation is of the first order. Three types of vibration modes are obtained, namely, the rigid body modes (cylindrical and conical), the torsional mode, and the first bending mode. The natural frequencies of the rigid body modes are given for both prototypes at speeds of about 1500–2000 rpm since these vibration modes are an interaction of the magnetic bearing stiffness and the rotor inertia and both prototypes have nearly similar masses (see Table 1) and the same magnetic bearing stiffness  $k_s$ . The radial bearing stiffness  $k_s$  was determined by simulation to be  $k_s = 20 \text{ N/mm}$ .

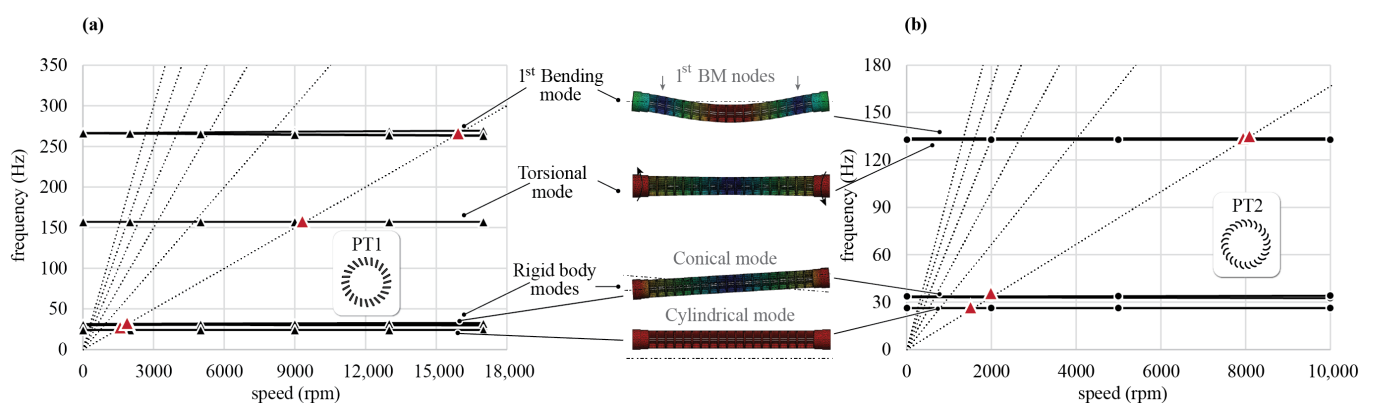


Figure 6. Simulated Campbell diagrams of (a) PT1 and (b) PT2.

The natural frequency of the torsional mode for PT1 lies between the natural frequencies of the solid and the first bending mode. For PT2, the torsional mode is just below the first bending mode.

The unbalance excitation of the first bending mode is expected to occur at 16,000 rpm for PT1 and at 8000 rpm for PT2. This suggests a significantly higher rotor stiffness of PT1

( $k_{\text{shaft,PT1}} > k_{\text{shaft,PT2}}$ ), as they have similar rotor masses. Additionally, the mode shape analysis shows that vibrational nodes are not located at the rotor shaft ends where the active magnetic bearing controls the rotor position for both PT1 and PT2. Therefore, the first bending resonance frequency will cause radial displacements within the bearings and thus be observable for the magnetic bearing in both prototypes.

From the modal analysis, it can be concluded that rigid, torsional and bending vibration modes can be excited in the targeted speed range and can exert destabilising forces on the magnetic bearing. The critical first bending mode will lead to radial displacements in the magnetic bearing of PT1 and PT2, whereby the stiff design of PT1 shifts the excitation to significantly higher speeds due to mass unbalance.

## 5. Fluid Dynamic Analysis

The goal of this section is to gain an understanding of the fluid dynamic properties of the CFF and the effects of design changes for the high-speed speed range using CFD simulations.

From a fluid dynamic point of view, the CFF is characterised by its complex, non-axisymmetric flow profile. It is defined by a double passage of air through the rotating blades and the formation of an eccentric vortex within the impeller [19–24]. In the literature, CFFs are referred to as “low-pressure fans” or “velocity generators”, as they do not generate high static pressure [25]. Generally, the energy increase created by a fan can be expressed as the sum of the increase in dynamic and static pressure

$$\Delta p_{\text{th}\infty} = \frac{\rho}{2} \left[ \overbrace{(c_2^2 - c_1^2)}^{\text{dynamic}} + \overbrace{(w_1^2 - w_2^2) + (u_2^2 - u_1^2)}^{\text{static}} \right] \quad (13)$$

as the first form of Euler’s fluid machine equation, where  $c$  is the absolute,  $u$  the circumferential, and  $w$  the relative velocity. Since the geometric sum of the circumferential and relative velocity gives the absolute velocity, the second form of Euler’s fluid machine equation [25] is obtained as

$$\Delta p_{\text{th}\infty} = \rho(u_2 \cdot c_{2u} - u_1 \cdot c_{1u}). \quad (14)$$

For a CFF, the fluid inlet and outlet are at the same rotor diameter ( $u_1 = u_2 = u$ ), such that the theoretical pressure increase can be written as

$$\Delta p_{\text{th}\infty} = \rho \cdot u \cdot \Delta c_u, \quad (15)$$

where  $\Delta c_u$  is the theoretical velocity deflection for an infinite number of blades. The total pressure increase is achieved by the deflection of the absolute velocity. How the velocity deflection occurs depends strongly on the impeller and casing geometry and is significantly influenced by the position, size, and intensity of the resulting eccentric vortex [26–28]. Analytical models are not able to accurately capture these aerodynamic features and loss mechanisms, so characteristic pressure–flow curves cannot be predicted. There are no conventional design procedures for CFFs; hence, the use of numerical methods is essential.

Therefore, a 2D simulation model was implemented that is robust in terms of numerical mesh and time step settings and provides a good compromise between computation time and resolution. The CFD model is described in the next section.

### 5.1. Numerical Method

The challenge in developing the CFD model lies particularly in the physics of the transient CFF flow. A sufficiently high resolution of the domain and the numerical time step was needed to reproduce the CFF flow, which is strongly dependent on the rotor and casing geometry. Furthermore, we determined that a comprehensive mesh and time step convergence study of the transient simulation should be conducted.

Figure 7a summarises the implemented steps for the creation and execution of the CFD simulations. Due to the uniform flow profile along the length of the CFF, cross-sectional planar 2D simulations were performed [27].

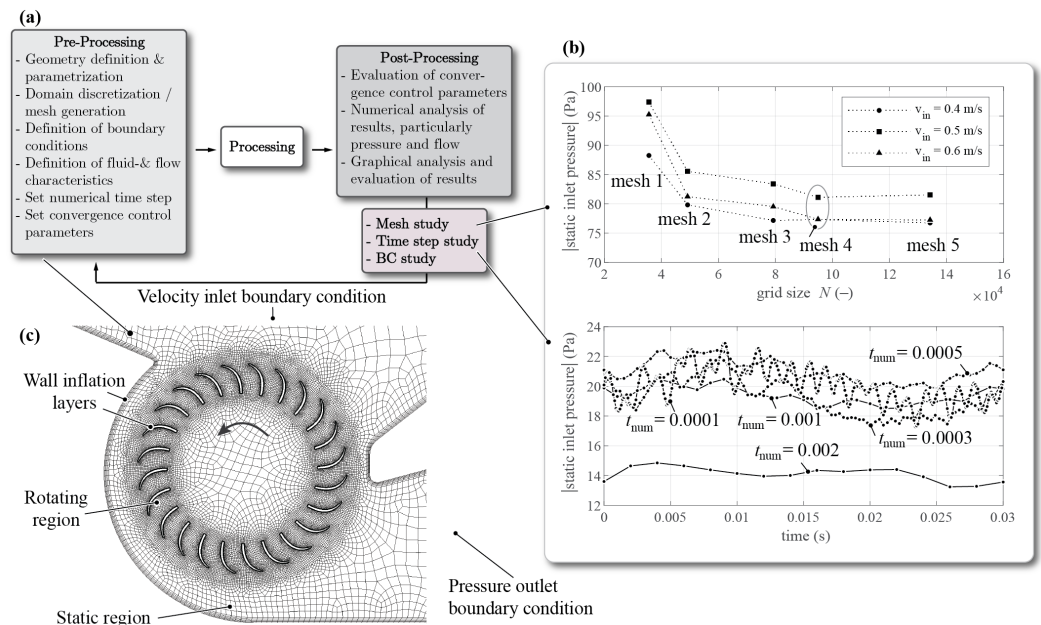


**Figure 7.** (a) Summary of the conducted pre-processing, processing, and post-processing steps for the development of the CFF CFD model. (b) Results of the mesh (top) and time step (bottom) sensitivity study. (c) Image of the resulting discretised domain in CFF region.

Three-dimensional effects are neglected due to the predominantly tangential flow fields. Moreover, the air (in a first step at room temperature, with a density  $\rho = 1.225 \text{ kg/m}^3$  and viscosity  $\mu = 1.7894 \cdot 10^{-5} \text{ kg/(m} \cdot \text{s)}$ ) was modelled as incompressible since the expected Mach numbers are below 0.3 (subsonic) and the CFF generates low pressures. Only high-flow operating points were simulated since the incompressible modelling of the air causes strong pressure fluctuations at low-flow operating points and thus does not represent the physical conditions well enough [27]. The sliding mesh method was used as the calculation approach, and the  $k - \omega$  SST model was used as the turbulence model.

Several mesh configurations,  $N$ , have been evaluated according to Figure 7b (top). The focus is placed on refinements in the rotating region, at the interface between rotating and static domain, and at the walls in order to sufficiently resolve velocity gradients. From mesh 4 onwards, an independent and robust mesh is obtained, with physical quantities remaining constant even with further increases in grid size,  $N$ . Figure 7c shows the discretised 2D domain in the CFF region. Furthermore, the boundary conditions reflect the relationship between the numerical simulation and the physical environment with a velocity inlet condition  $v_{in}$  and a static outlet pressure of  $p_{stat,out} = 0 \text{ Pa}$  (relative to the ambient pressure). By varying the velocity inlet condition, different operating points can be simulated.

A detailed sensitivity study with respect to the numerical time step  $t_{num}$  was performed, which is shown in Figure 7b (bottom). It resulted in a speed-dependent time step of 0.015 rotor turns, e.g., for 3000 rpm, the time step was set to 0.0003 s.

In summary, the resulting 2D simulation model is robust in terms of numerical mesh and time step settings and offers a good trade-off between computation time and resolution. It can be used to simulate various rotor geometries at different speeds and operating points.

## 5.2. Results of Simulation

Figure 8a shows the velocity and pressure profiles resulting from the CFD simulation for PT1, and those for PT2 are shown in Figure 8b. The velocity vectors show the inflow

and outflow regions and the characteristic non-axisymmetric flow profile of both PTs. As expected, the air passes each fan blade twice, first as it enters the fan impeller and then again as it exits. The eccentric vortex is shown in the pressure profiles for both PTs. Thus, the implemented CFD simulation allows a successful visual representation of the CFF pressure and flow characteristics. The comparison of straight (PT1) and curved (PT2) blades show that at the same rotational speed and at a high-flow operating point, the velocities at the outlet of PT2 are significantly higher.

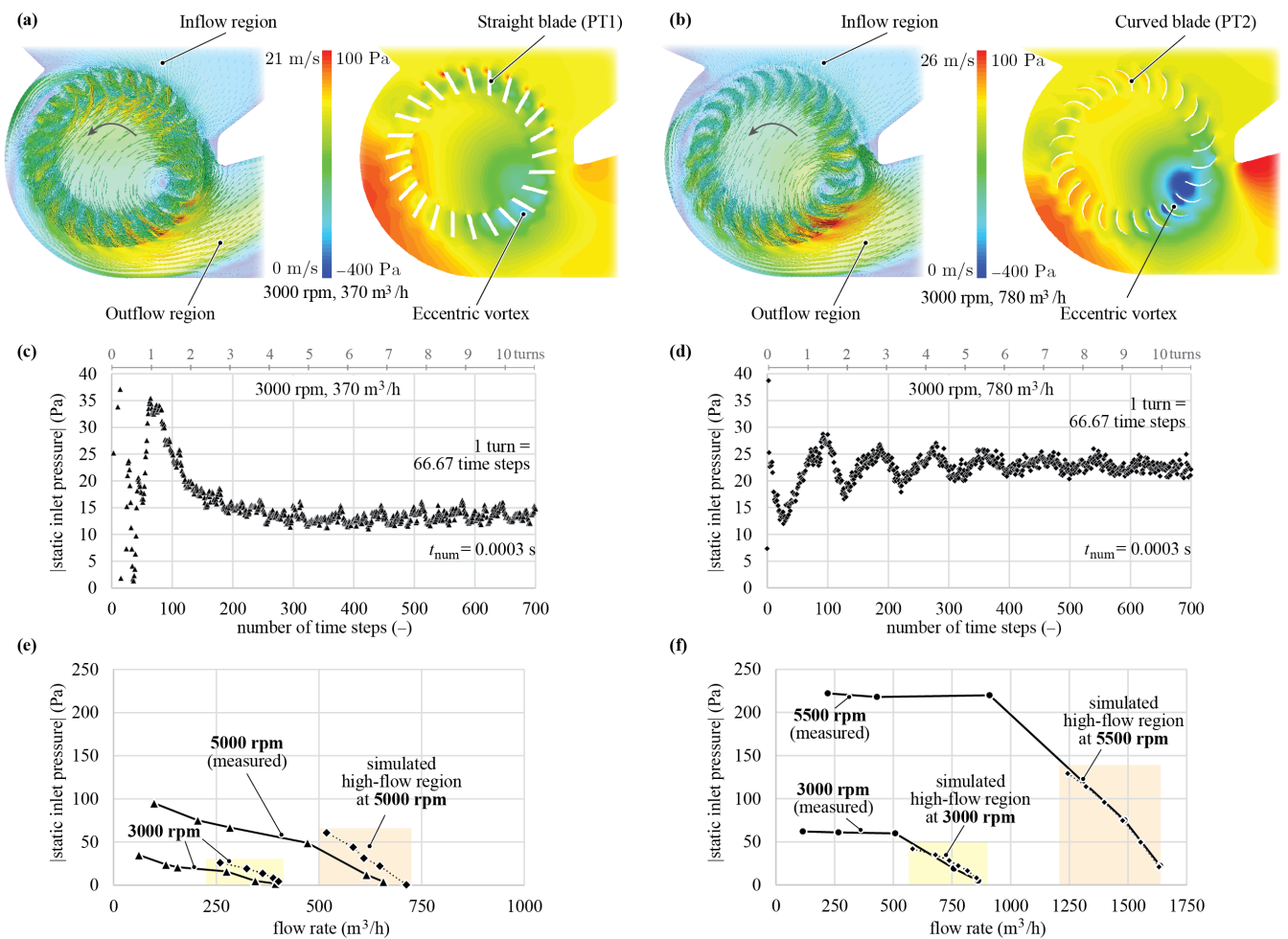


**Figure 8.** CFD-simulated velocity and pressure profile of (a) PT1 and (b) PT2 for a high-flow operating point at 3000 rpm. The characteristic flow features are shown for both PTs. Convergence study evaluating the control points (absolute value of static inlet pressure) over the number of numerical time steps for PT1 in (c) and for PT2 in (d). Comparison of the experimentally and simulatively determined pressure–flow characteristics for PT1 in (e) and for PT2 in (f).

Furthermore, Figure 8c,d illustrates the absolute value of the static inlet pressure versus the number of conducted numerical time steps (for the same operating point as in Figure 8a,b). This demonstrates a successful convergence after approximately six turns, as a 360° rotation of the fan blades corresponds to 66.67 time steps.

In Figure 8e,f, different operating points are simulated for different speeds and compared with those experimentally determined (see Section 6). To obtain the flow rate from the 2D simulation, the inlet velocity was multiplied by the effective fluid inlet length (see  $L_{fluid}$  in Table 1) and the height of the channel (see  $h_{channel}$  in Section 6). For the high flow speed curves of PT2 in Figure 8f, the simulated and measured points agree very well. However, in Figure 8e, it can be seen that the simulated speed curves of PT1 are higher

than the measured ones. This deviation could originate from wall boundary conditions and loss mechanisms that occur at the flow inlet and outlet of PT1, which consist of several individual inlet surfaces in the axial direction but are not represented in the planar 2D simulation. Furthermore, it could stem from manufacturing tolerances as the CFF's performance is strongly dependent on the slope of the fan blades.

Different blade slopes have been simulated for the milled PT1 for a blade thickness of 1.4 mm, as predefined by the manufacturing process. The simulated high-flow operating points for a slope of 14°, 16° (PT1), and 18° are shown in Figure 9c. The velocity and pressure profiles for blades with a slope of 14° (steeper than PT1) are shown in Figure 9a and of 18° (flatter than PT1) in Figure 9b. An influence of the blade angle on the velocity and pressure distributions can be seen. The simulations have shown that if the blade slope is too steep, there is a higher impact pressure on the blades at the inlet side (pressure loss), resulting in a reduced deflection of the absolute velocity on the outlet side. If the blade slope is too flat, the air supply into the fan is blocked more on the inlet side, which has negative consequences on the dynamic pressure supplied to the flow on the outlet side. The geometry of PT1 resulted from iteratively varying the slope of the blades for a given inner diameter  $d_i$ , outer diameter  $d_o$ , and blade thickness  $t_{PT1}$  and has shown the best flow characteristics for 16°.

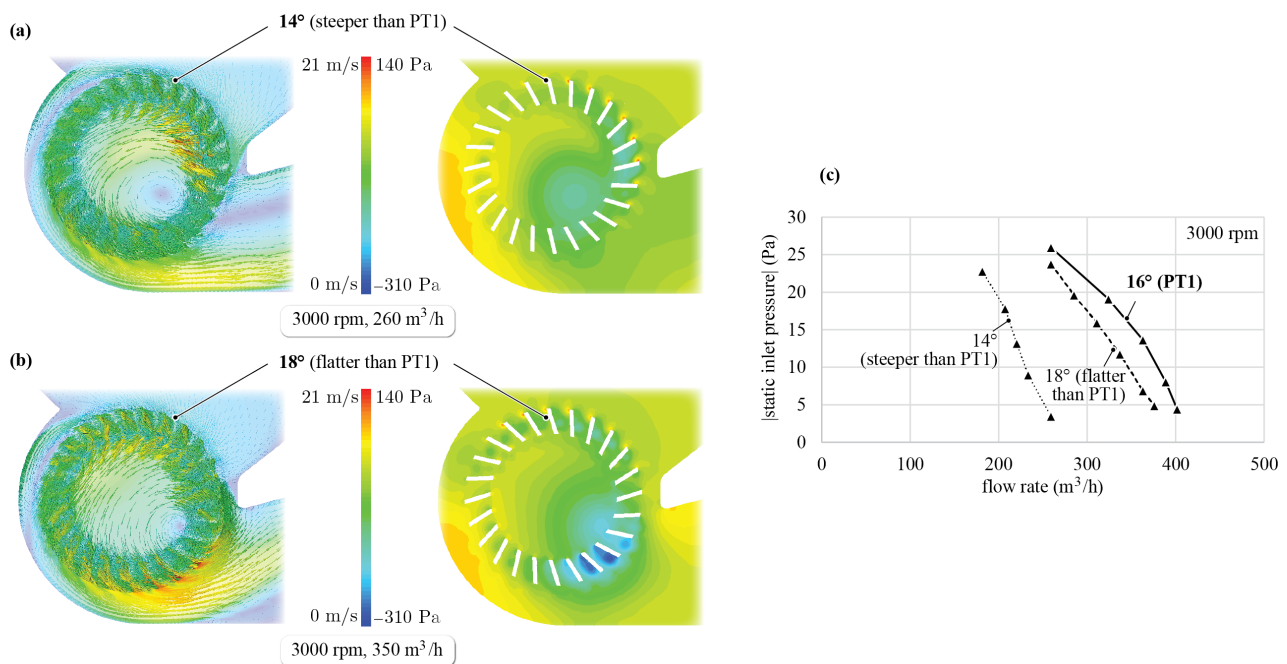


**Figure 9.** Velocity and pressure profiles for straight blades with slope of (a) 14° and (b) 18°. (c) Simulative comparison of straight blades with three different slopes.

## 6. Experimental Analysis

For the experimental CFF study, all measurements were performed with air under ambient pressure. For other operating conditions, e.g., higher gas density in an excimer laser chamber, a conversion would be possible using the linear relationship between pressure difference and density as  $\Delta p_{\text{excimer}} \propto \Delta p_{\text{air}} \cdot \rho_{\text{excimer}} / \rho_{\text{air}}$ . The test rig that is shown schematically in Figure 10c was designed. The flow into the CFF was guided through a 4.5 m long ventilation duct, with free flow exiting the CFF. At the duct inlet, an exchangeable grid set the load curve, i.e., it defined a certain operating point. A flow straightener then ensured that the flow was directed and the velocity measurement was accurately measured by the thermal flow sensor. The static pressure measurement took place before the fan.

To investigate the velocity distribution in the ventilation duct, the velocity was measured across the width at different locations. The velocity profile can be seen in Figure 10a. From this, the profile factor of the flow could be calculated according to

$$PF = \frac{v_{avg}}{v_s}, \quad (16)$$

where  $v_s$  is the velocity at the sensor in the centre of the duct and  $v_{avg}$  is the mean velocity. The flow rate then resulted from multiplying  $v_s$  by the profile factor and the duct area with

$$Q = v_s \cdot PF \cdot h_{channel} \cdot b_{channel}. \quad (17)$$

For this test rig, a profile factor of 0.92 was obtained.

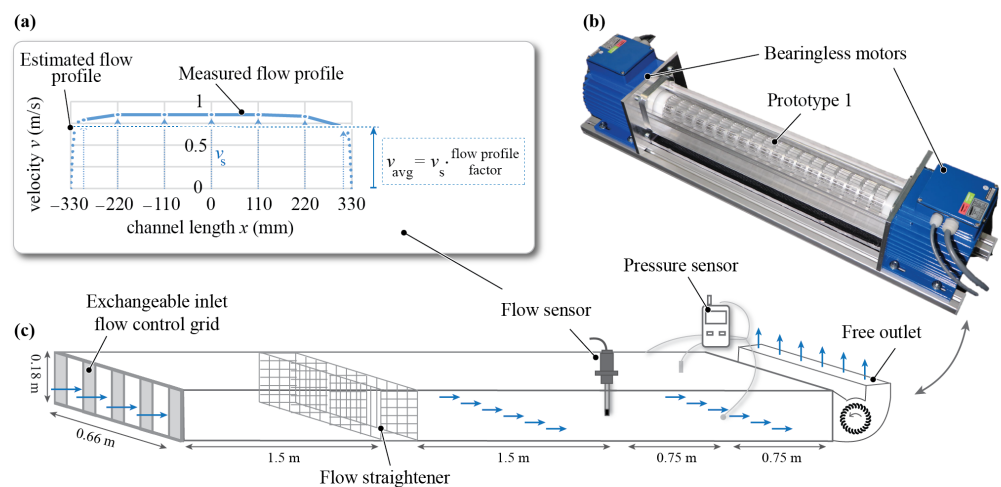


**Figure 10.** (a) Velocity profile measured with the flow sensor in the centre of the ventilation duct at different channel width positions. (b) Image of the entire high-speed bearingless CFF system with PT1. (c) Schematic of the designed test rig with inlet grid, flow straightener, flow sensor, and pressure sensor. The flow into the CFF is ducted, while the flow exits freely from the fan into the environment.

### 6.1. Position Measurements of Rotor Magnets

The magnetic bearing must be able to withstand the rotor and fluid dynamic forces, as discussed in Section 4. The aim of these measurements was to determine which maximum rotational speeds could be achieved with the independent position control structure of BM1 and BM2 and what the present limitations were. The displacements of the rotor magnet in the magnetic bearing were evaluated and were measured via built-in sensors in the bearingless motor.

Figure 11a shows the measured radial displacements of the rotor magnet for BM1 and BM2 at different speeds of PT1, and those of PT2 are shown in Figure 11b. The measurements were carried out for each speed for two operating points, namely at maximum (“max flow”) and minimum (“no flow”) flow. The rigid body modes simulated in Figure 6 did not pose a problem for the magnetic bearing since a “force-rejection” algorithm was implemented in the position control [18]. This unbalanced control strategy can be interpreted as a generalised notch filter. This shifted the axis of rotation of an unbalanced rotor from the geometric centre of gravity to the centre of mass, such that the rotor rotated in a completely force-free manner. Thus, no rigid body modes could be excited by the unbalance. Furthermore, the forces generated by the air flow (no-flow versus max flow points in Figure 11a,b) had no measurable/no significant influence on the rotor displacement in the magnetic bearing. Therefore, we considered them to be neglectable. The predicted torsional mode was also not excited during the measurements and did not lead to any destabilising forces.

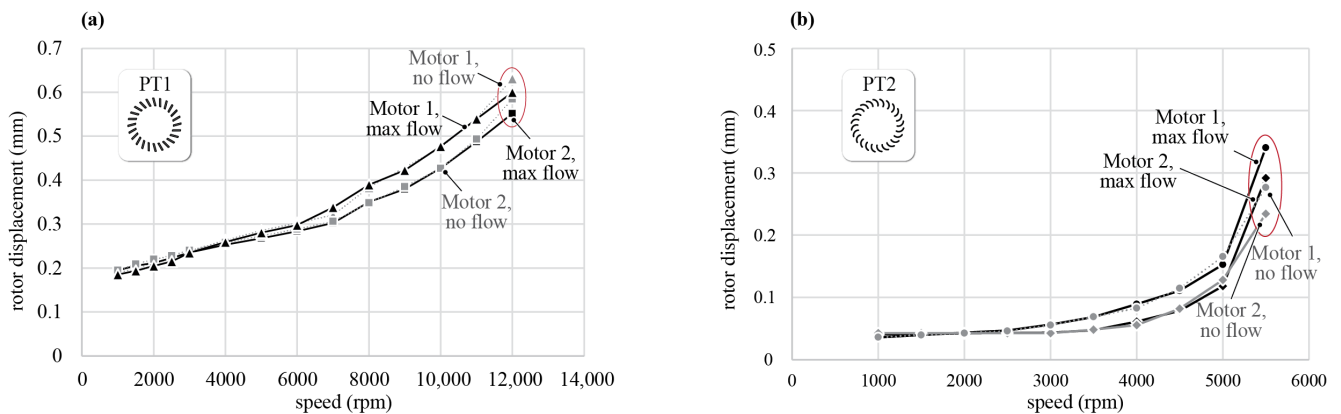


**Figure 11.** Measured radial rotor displacements in the magnetic bearing of (a) PT1 and (b) PT2.

In contrast, the first bending mode occurred for both rotors. In Figure 11b, the quickly increasing radial displacements of the less stiff CFF are clearly visible. Stroboscopic measurements optically confirmed the bending of the rotor. With the present control structure, the first bending resonance frequency could not be passed, meaning that PT2 could only operate subcritically—but stably—up to 5500 rpm. The critical speed of the first bending mode of 8000 rpm simulated in Figure 6b most likely overestimates the mechanical stiffness due to the multi-body nature of the prototype and the imperfectly bonded connections between the individual components, which is why the first bending resonance frequency occurs earlier in the measurement.

PT1 was successfully operated up to 12,000 rpm (see Figure 11a). Due to the large air gap offered by the bearingless motor (as explained in Section 2), large displacements, and thus, high speeds, can be allowed with the “force-rejection” algorithm. The simulated bending resonance frequency of 15,500 rpm from Figure 6b also occurred earlier with PT1 and could not be passed.

The higher displacements of PT1 compared to PT2 at low speeds indicated a higher mass unbalance. Although balancing can reduce the displacements up to the resonance frequency, it is still not possible to pass the critical speed. In addition, it can be concluded from both diagrams that the radial displacements are approximately the same at maximum and minimum flow, which means that the rotor dynamic forces dominate over the fluidic forces.

For both PTs, the first bending resonance frequency currently represents the limit for the magnetic bearing of the bearingless motor, which is why both PTs could only be operated subcritically.

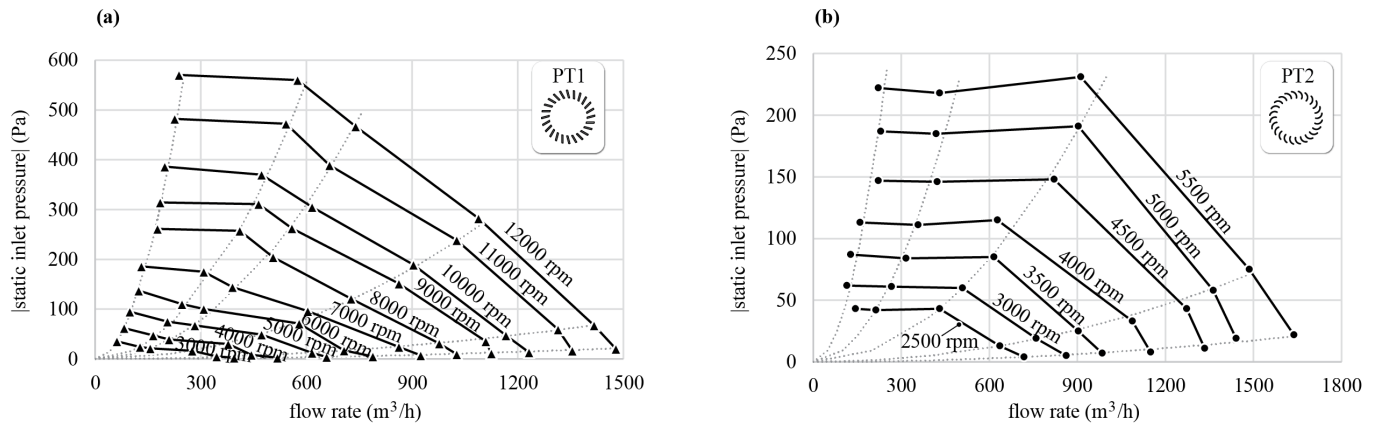
## 6.2. Pressure–Flow Curves

Figure 12a shows the characteristic pressure–flow curves of PT1. This CFF reached a maximum speed of 12,000 rpm with a maximum flow rate of approximately  $1450 \text{ m}^3 \text{ h}^{-1}$ . Figure 12b shows the pressure–flow characteristics of PT2, resulting in a flow of approximately  $1600 \text{ m}^3 \text{ h}^{-1}$  at the maximum achieved speed of 5500 rpm. The comparison of PT1 and PT2 shows experimentally that the robust design of PT1 allows for high speeds, but there is a loss in flow rate. This results from the shorter effective fluid inlet length (see Table 1) in combination with the straight blade profiles.

Comparing the fluid performance (the multiplication of pressure increase and flow rate) at maximal speed for PT1 and PT2, PT1 generates a higher performance for operating points with higher resistance. Depending on the resistance of the heat exchangers in the excimer laser application, this can be advantageous.

Overall, PT2 performs better from a maximal flow point of view, but the low shaft stiffness and the excitation of the first bending resonance frequency do not allow higher

speeds than 5500 rpm, while the robust design of PT1 allowed rotational speeds up to 12,000 rpm and thereby led to a fluid performance increase for operating points with higher resistance, e.g., from the heat exchangers.



**Figure 12.** Pressure–flow curves measured in the presented test rig for (a) PT1 up to 12,000 rpm and (b) PT2 up to 5500 rpm.

## 7. Conclusions

In this study, a comparative evaluation of two bearingless cross-flow fan designs was performed. Two prototypes were designed, optimised, and analysed in terms of their rotor dynamic and fluid dynamic performance and pushed towards high-speed and high-performance operation. For the target application in DUV lithography excimer lasers, the bearingless CFF concept allows for a simple, hermetically sealed and conveniently maintainable and exchangeable placement of the drives outside the laser chamber. An increase in CFF speed and thus flow has a direct impact on the throughput and scan speeds of these systems.

This study addresses the trade-off and complex interactions between the mechanical strength, fluid dynamic performance, and manufacturability of the CFF rotor and the consequent impact on the magnetic bearing and maximum achievable speed. For this purpose, two prototypes were successfully commissioned and investigated by FEM and experimental measurements. The performed modal analysis allowed an estimation of expected vibration modes, particularly the critical speed of the first bending mode and its node location. With the presented CFD simulation, a visualisation of local flow effects along the blade geometries, as well as a CFF design comparison, was accomplished.

PT1 represents an easily manufacturable and stiff rotor that could be operated up to 12,000 rpm. This demonstrated that stable operation up to the first bending resonance frequency in this high-speed range is possible with the current position control structure. At maximal speed, PT1 resulted in higher fluid power for operating points with higher resistance compared to PT1. However, the robust design comes at the expense of a limited fluid flow.

PT2 performs much better from a fluid dynamic point of view, but the more flexible design limits the maximum achieved speed to 5500 rpm due to the excited first bending resonance frequency.

It can be concluded that the magnetic bearing can only handle forces and allow deflections to a limited extent and that the first bending resonance frequency currently limits the position control of the bearingless motor presented here. Future research will focus on passing the critical speed to obtain a better trade-off between rotational speed and fluid performance with the same unique technical advantages that the bearingless CFF technology currently offers.

**Author Contributions:** Conceptualization, I.B., D.S. and T.N.; methodology, I.B., R.H. and D.S.; investigation and validation, I.B.; writing—original draft preparation, I.B.; writing—review and editing, I.B., R.H., D.S., T.N. and J.W.K.; supervision, D.S. and J.W.K.; project administration, J.W.K. All authors have read and agreed to the published version of the manuscript.

**Funding:** This research was funded by the Swiss Innovation Agency Innosuisse.

**Data Availability Statement:** Data presented in this study are available on request from the corresponding author. The data are not publicly available due to internal policies of the industry research partner.

**Acknowledgments:** The authors gratefully thank the Swiss Innovation Agency Innosuisse for their financial support and Levitronix GmbH for their financial, scientific, and technical contributions.

**Conflicts of Interest:** The authors declare no conflict of interest.

## References

1. Basting, D.; Marowsky, G. *Excimer Laser Technology*; Springer: Berlin/Heidelberg, Germany, 2005; ISBN 978-3-642-05749-6.
2. Basting, D.; Pippert, K.D.; Stamm, U. History and future prospects of excimer lasers. In Proceedings of the 2nd International Symposium on Laser Precision Microfabrication, Singapore, 16–18 May 2001 <https://www.spiedigitallibrary.org/conference-proceedings-of-spie/4426.toc>.
3. Borisov, V.M.; Vinokhodov, A.Y.; Vodchits, V.A.; Demin, A.I.; El'tsov, A.V.; Basting, D.; Stamm, U.; Voss, F. Compact 600-W KrF laser. *Quantum Electron.* **1998**, *28*, 119–122. [[CrossRef](#)]
4. Borisov, V.M.; Vinokhodov, A.Y.; Vodchits, V.A.; El'tsov, A.V.; Ivanov, A.S. Development of high-power KrF lasers with a pulse repetition rate up to 5 kHz. *Quantum Electron.* **2000**, *30*, 783–786. [[CrossRef](#)]
5. Borisov, V.M.; Vinokhodov, A.Y.; Vodchits, V.A.; El'tsov, A.V. On ultimate pulse repetition rates of an XeF laser. *Quantum Electron.* **2000**, *30*, 881–883. [[CrossRef](#)]
6. Das, P.; Sandstrom, R.L. Advances in excimer laser technology for sub-0.25- $\mu\text{m}$  lithography. *Proc. IEEE* **2002**, *90*, 1637–1652. [[CrossRef](#)]
7. Sarkar, K.; Ujazdowski, R.C.; Das, P.P.; Larson, D.G. Excimer Laser with Magnetic Bearings Supporting Fan. U.S. Patent 5,848,089, 8 December 1998.
8. Sekiguchi, S.; Shinozaki, H.; Aiyoshizawa, S.; Barada, T.; Ooyama, A. Magnetic Bearing and Circulation Fan Apparatus. U.S. Patent 6,519,273, 11 February 2003.
9. Miki, M.; Wakabayashi, O. Gas Laser Apparatus and Magnetic Bearing Control Method. U.S. Patent 11,162,530, 2 November 2021.
10. Sun, X.; Chen, L.; Yang, Z. Overview of bearingless permanent-magnet synchronous motors. *IEEE Trans. Ind. Electron.* **2013**, *60*, 5528–5538. [[CrossRef](#)]
11. Warberger, B.; Kaelin, R.; Nussbaumer, T.; Kolar, J.W. 50-N · m/2500-W Bearingless motor for high-purity pharmaceutical mixing. *IEEE Trans. Ind. Electron.* **2012**, *59*, 2236–2247. [[CrossRef](#)]
12. Chen, J.; Zhu, J.; Severson, E.L. Review of bearingless motor technology for significant power applications. *IEEE Trans. Ind. Appl.* **2019**, *56*, 1377–1388. [[CrossRef](#)]
13. Gruber, W.; Bauer, W.; Wetsch, D.; Wex, B.; Kurita, N. Implementation of a bearingless axial-force/torque motor fan with flex-PCB windings. In Proceedings of the IEEE International Electric Machines & Drives Conference, San Diego, CA, USA, 12–15 May 2019; pp. 179–184. [[CrossRef](#)]
14. Osa, M.; Masuzawa, T.; Yamaguchi, K.; Tatsumi, E. Double Stator Axial Gap Type Ultra-Compact 5-DOF Controlled Self-bearing Motor for Rotary Pediatric Ventricular Assist Device. *IEEE Trans. Ind. Appl.* **2021**, *57*, 6744–6753. [[CrossRef](#)]
15. Bagaric, I.; Steinert, D.; Wassmer, F.; Holenstein, T.; Nussbaumer, T.; Kolar, J.W. Design and characterization of a bearingless cross-flow fan. In Proceedings of the IEEE/ASME International Conference on Advanced Intelligent Mechatronics (AIM), Delft, The Netherlands, 12–16 July 2021; pp. 1195–1200. [[CrossRef](#)]
16. Steinert, D.; Nussbaumer, T.; Kolar, J.W. Slotless bearingless disk drive for high-speed and high-purity applications. *IEEE Trans. Ind. Electron.* **2014**, *61*, 5974–5986. [[CrossRef](#)]
17. Gasch, R.; Nordmann, R.; Pfützner, H. *Rotordynamik*; Springer: Berlin/Heidelberg, Germany, 2006; ISBN 3-540-41240-9.
18. Schweitzer, G.; Maslen, E.H. *Magnetic Bearings*; Springer: Berlin/Heidelberg, Germany, 2009; ISBN 978-3-642-10153-3.
19. Toffolo, A. On the theoretical link between design parameters and performance in cross-flow fans: A numerical and experimental study. *Comput. Fluids* **2005**, *34*, 49–66. [[CrossRef](#)]
20. Shih, Y.C.; Hou, H.C.; Chiang, H. On similitude of the cross flow fan in a split-type air-conditioner. *Appl. Therm. Eng.* **2008**, *28*, 1853–1864. [[CrossRef](#)]
21. Dang, T.Q.; Bushnell, P.R. Aerodynamics of cross-flow fans and their application to aircraft propulsion and flow control. *Prog. Aerosp. Sci.* **2009**, *45*, 1–29. [[CrossRef](#)]
22. Li, Y.; Ouyang, H.; Tian, J.; Du, Z.; Zheng, Z. Experimental and numerical studies on the discrete noise about the cross-flow fan with block-shifted impellers. *Appl. Acoust.* **2010**, *71*, 1142–1155. [[CrossRef](#)]

23. Ouyang, H.; Tian, J.; Li, Y.; Zheng, Z.; Du, Z. Internal flow and noise investigations about the cross-flow fan with different blade angles. *J. Turbomach.* **2012**, *134*, 051023. . [[CrossRef](#)]
24. Zhang, W.; Yuan, J.; Si, Q.; Fu, Y. Investigating the In-Flow Characteristics of Multi-Operation Conditions of Cross-Flow Fan in Air Conditioning Systems. *Processes* **2019**, *7*, 959. [[CrossRef](#)]
25. Eck, B. *Ventilatoren*; Springer: Bergin/Heidelberg, Germany, 1972; ISBN 3-540-05600-9.
26. Lazzarotto, L.; Lazzaretto, A.; Martegani, A.D.; Macor, A. On cross-flow fan similarity: Effects of casing shape. *J. Fluids Eng.* **2001**, *123*, 523–531. [[CrossRef](#)]
27. Dornstetter, S. Numerische und experimentelle Untersuchungen an Querstromventilatoren. Ph.D. Dissertation, Karlsruhe Institute of Technology, Karlsruhe, Germany, 2002.
28. Lazzaretto, A. A criterion to define cross-flow fan design parameters. *J. Fluids Eng.* **2003**, *125*, 680–683. [[CrossRef](#)]

**Disclaimer/Publisher’s Note:** The statements, opinions and data contained in all publications are solely those of the individual author(s) and contributor(s) and not of MDPI and/or the editor(s). MDPI and/or the editor(s) disclaim responsibility for any injury to people or property resulting from any ideas, methods, instructions or products referred to in the content.